

A New Compact Model For High-Performance Tunneling-Field Effect Transistors

Ramon B. Salazar^{§,*}, Hesameddin Ilatikhameneh^{†,*}, Rajib Rahman[†], Gerhard Klimeck[†], and
Joerg Appenzeller[§]

§ Birck Nanotechnology Center, Purdue University, 1205 W. State Street, West Lafayette, IN 47907, IN, USA.

† Network for Computational Nanotechnology, 207 S. Martin Jischke Drive, West Lafayette, IN 47907, IN, USA.

* These two authors contributed equally to this work.

Keywords: *Tunneling-Field Effect Transistor, Tunneling, Tunnel-FET, Analytic Model, NEGF, ballistic, quantum transport.*

AUTHOR INFORMATION

Corresponding Authors:

E-mail: ramon@purdue.edu, hilatikh@purdue.edu

Abstract.-

A new analytic compact model is presented which describes the full current-voltage (I-V) characteristic of ballistic high-performance (aggressively scaled-down) tunneling field-effect-transistors (TFETs) based on direct-bandgap semiconductors. The model is based on an analytic description of two key features, which capture the main physical phenomena related to TFETs: 1) the potential profile along the channel including the impact of doping concentration in the source, and 2) the evanescent states in the bandgap region of the semiconductor including the ellipticity of the imaginary branch. The analytic description of the potential profile is made using two different approaches. One of them is based on a piecewise function derived from the Poisson's equation in the source and channel, and the other is an ad-hoc potential that describes accurately

the tunneling distance. The compact model is validated by comparison with state-of-the-art quantum transport simulations using a full band atomistic approach. Both approaches proposed to describe the potential profile are found in good agreement with the data from the simulations in all regions of operation: the on/off states and both n/p branches of conduction. It is shown that as TFETs are scaled-down the impact of source/drain doping on device performance becomes crucially relevant. In addition, it is shown how this model can be used to calculate the energy-dependent band-to-band tunneling (BTBT) currents in TFETs, a feature that allows gaining deep insights into the underlying device physics. The simplicity and accuracy of the model provides a powerful tool to explore in a quantitatively manner how a wide variety of parameters (material-, size- and/or geometry-dependent) impact the TFET performance under any bias conditions. The proposed model presents thus a practical complement to computationally expensive simulations such as the state-of-the-art 3D Non-Equilibrium Green's Function (NEGF) approach.

1- Introduction

Tunneling field-effect-transistor (TFET) are considered one of the attractive device concepts in the field of nanoelectronics¹. TFETs have the potential ability to perform with an inverse subthreshold slope (S) smaller than conventional thermionic emission-based devices that exhibit S -values above 60mV/dec at room-temperature. This advantage translates in particular into low-voltage operation and may – for the right choice of band gap material – result in low stand-by power dissipation, making TFETs a more energy-efficient device if compared to complementary metal-oxide-semiconductor (CMOS) FETs¹⁻⁷.

However, in order to be able to compete with CMOS devices, TFETs must be carefully designed not only to operate with a small S , but also to show high on-state currents (I_{on})¹. The development of analytical models for TFETs is of great importance in this context since those models allow optimizing the transistor design by gaining an in-depth understanding of how to tune the key parameters to enable high performance devices.

In this work, it is shown that in the case of TFETs whose channel material consists of direct bandgap semiconductors with a single dominant tunneling path, the current vs. channel-potential characteristics of the device can be described by combining analytic models which capture: a) the effective band bending distance from source to channel (Λ_{S-CH}) which takes into account the impact of doping in the source/drain regions, and b) the elliptic curvature of the complex band structure, which describes the tunneling of electrons and holes through the band gap. It is shown in particular that aggressively scaled down TFETs for high-performance applications are impacted more by the depletion width in the source/drain regions than by the geometric screening length, which is in turn captured by the analytic expressions. The proposed model provides results, which are in good agreement with those obtained through rigorous numerical calculations using the self-consistent Poisson-Non-Equilibrium Green's Function (NEGF) methodology in our simulation engine NEMO5.

2.- Theory.

2.1 The Effective Screening Length

Theoretical studies are frequently concerned with homojunction TFETs with a heavily doped source and a lightly doped (or intrinsic) channel⁸⁻¹³ and assume that an “*effective screening length*” (Λ_{S-CH}) describes the total band bending distance from source to channel (see Fig. 1). Moreover, it is often assumed that the source is doped to such a high extent that there is almost no depletion (or band bending) in this region and thus $\Lambda_{S-CH} \approx \lambda_{ch}$ as shown in Fig. 1a (λ_{ch} is the *geometric*

screening length of the gated semiconductor¹⁴⁻¹⁶, e.g. $\lambda_{ch} = \sqrt{\frac{\epsilon_{body} t_{body}^2}{\epsilon_{ox} 8} \ln\left(1 + \frac{2t_{ox}}{t_{body}}\right) + \frac{t_{body}^2}{16}}$ for a

cylindrical geometry). Previous reports have discussed how neglecting the band bending inside the source/drain regions leads to an overestimation of the electric field at the source/channel (and channel/drain) junction¹⁷. In this work it will be shown that for high-performance devices (aggressively scaled-down) where λ_{ch} is very small, neglecting the band bending in the

source/drain regions indeed leads to significantly overestimated on-currents of band-to-band (BTB) TFETs.

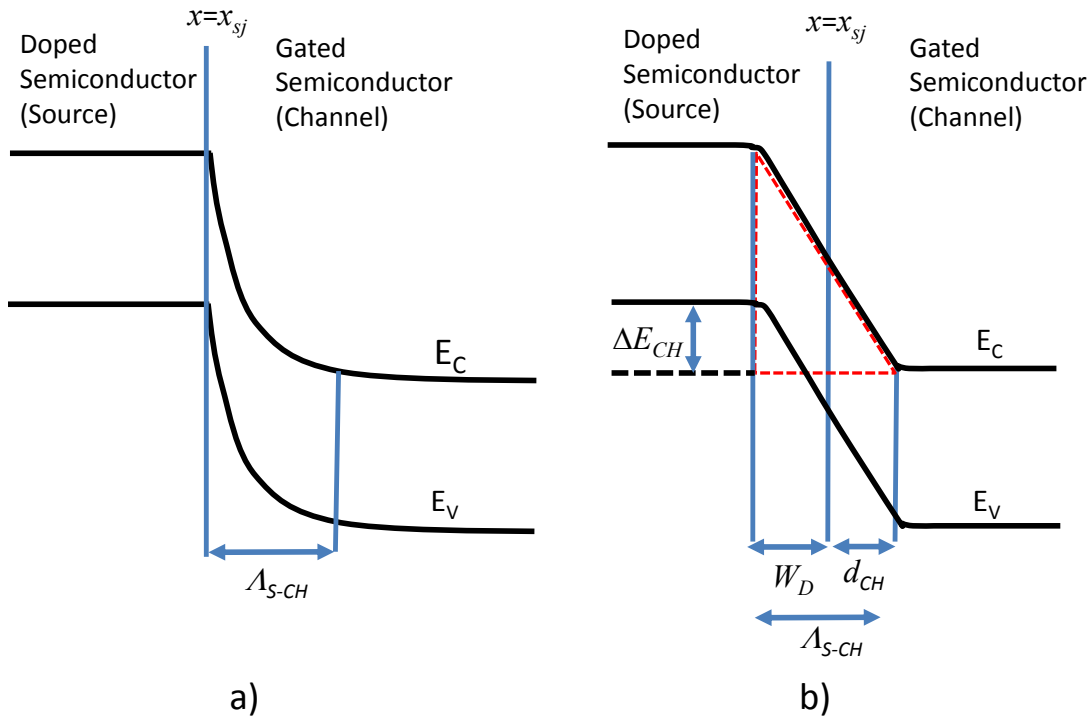


Figure 1. Schematics of the potential profile along the channel of a homojunction TFET assuming **a)** infinite doping level in the source and **b)** finite doping in the source. The point $x = x_{sj}$ defines the source/channel interface.

A more appropriate description of the electrostatics in the homojunction leads to a potential profile as shown in Fig. 1b (the point $x = x_{sj}$ defines the source/channel interface). In this case, band bending exists inside the gated channel as well as in the source region. Thus, the total band bending distance from source to channel “ Λ_{S-CH} ” is given by the sum of d_{ch} (the distance associated with band bending inside the gated channel) and the depletion width “ W_D ” (the distance associated with band bending in the source).

2.2 Analytic Description of the Potential Profile

Finding an analytic solution to the full 3D-Poisson equation from source to channel to describe the potential profile and the electric field is a non-trivial task. In this work, two different approaches are proposed to solve this problem in a simpler way. These approaches are described as follows.

In the doped source far from the source-channel interface the Poisson equation can be written as:

$$\frac{d^2 U_S}{dx^2} = -\frac{qN_S}{\epsilon} . \quad (1)$$

where q is the elementary charge of the electron, and U_S , N_S , and ϵ are: the potential in the source (or drain) region, the corresponding doping concentration in the source (or drain), and the in-plane permittivity of the semiconductor in that region respectively. In contrast, far from the source/channel interface the Poisson equation for the channel potential “ U_{ch} ” can be written as¹⁴:

$$\frac{d^2 U_{ch}}{dx^2} = \frac{U_{ch}}{\lambda_{ch}^2} . \quad (2)$$

Self-consistent numerical simulations of the 3D Poisson-transport equations reveal the following:

- 1- The first derivative of the potential must be continuous from source to channel.
- 2- Inside the gated channel and far from the interface, the potential approaches the value of potential in the channel.
- 3- Inside the source region and far from the interface, the potential approaches the value of the potential in the source.

2.2.1 Continuous Piecewise Analytic potential

The general forms of the solutions to (1) and (2) are given by $U_S(x) = \frac{A}{2}(x - x_{Sj} + W_D)^2$ and $U_{ch}(x) = (\phi_j - \phi_{ch})\exp\left(-\frac{x-x_{Sj}}{\lambda_{ch}}\right) + \phi_{ch}$ respectively¹⁷, where A is a constant and W_D is the depletion width in the source region, ϕ_j is the potential at the source/channel junction, and ϕ_{ch} is the potential at the channel as shown in Fig. 2. As an approximation, it is assumed that the solutions

to (1) and (2) are still valid in the region close to the source/channel interface. Taking this into account, the value of ϕ_j can be found by satisfying continuity of the electric field at the junction.

Therefore, by making $\left. \frac{\partial U_{ch}}{\partial x} \right|_{x=x_{sj}} = \left. \frac{\partial U_S}{\partial x} \right|_{x=x_{sj}}$ and by noting that $U_S(x_{sj}) = \frac{A}{2}(W_D)^2 = (\phi_j - \phi_s)$

where ϕ_s is the potential at the source (see Fig. 2b) the following expression can be obtained:

$$\frac{(\phi_j - \phi_s)}{\frac{W_D}{2}} = -\frac{(\phi_j - \phi_{ch})}{\lambda_{ch}} \quad (3)$$

Solving for ϕ_j in (3) allows to find expressions for A and $(\phi_j - \phi_{ch})$:

$$\frac{A}{2} = \frac{\frac{W_D}{2}}{\lambda_{ch} + \frac{W_D}{2}} \frac{(\phi_s - \phi_{ch})}{W_D^2}, \quad (4)$$

$$(\phi_j - \phi_{ch}) = \frac{\lambda_{ch}}{\lambda_{ch} + \frac{W_D}{2}} (\phi_s - \phi_{ch}). \quad (5)$$

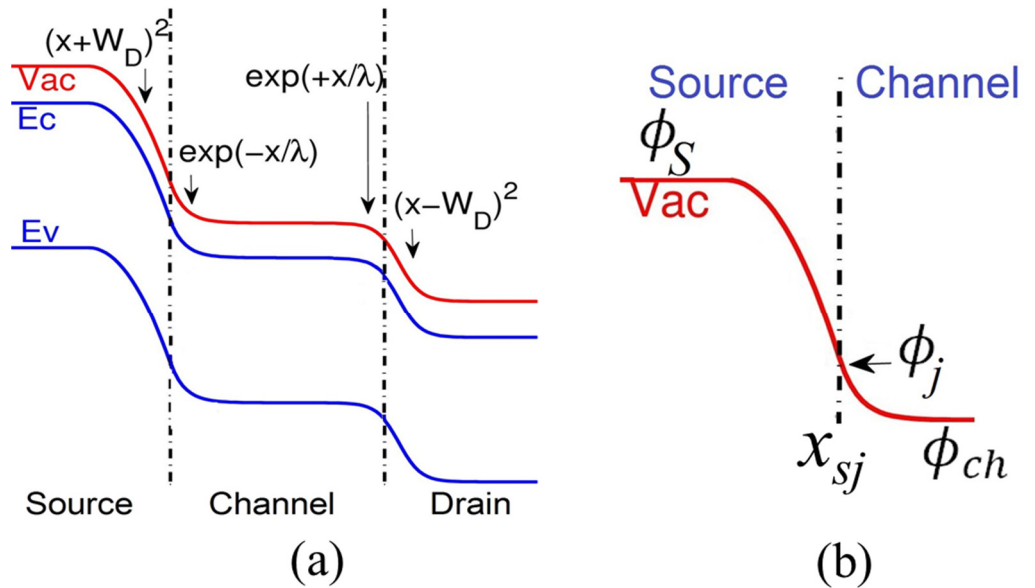


Figure 2. a) Band diagram of a TFET showing the general form of the analytic solutions. b) The source-channel potential profile with relevant symbols. The conduction and valence band edges are given by the electrostatic potential ($E_c(x) = U_{vac}(x) - \chi(x)$, $E_v(x) = E_c(x) - E_g(x)$).

In this way, the solutions to (1) and (2) are rewritten using expressions (4) and (5) which leads to the full continuous piecewise analytic potential profile from source to channel denoted as $U_P(x)$:

$$U_P(x) \approx \begin{cases} \phi_s & x < x_{Sj} - W_D \\ \phi_s - \frac{\frac{W_D}{2}}{\lambda_{ch} + \frac{W_D}{2}} (\phi_s - \phi_{ch}) \frac{(x - x_{Sj} + W_D)^2}{W_D^2} & x_{Sj} - W_D < x < x_{Sj} \\ \phi_{ch} + \frac{\lambda_{ch}}{\lambda_{ch} + \frac{W_D}{2}} (\phi_s - \phi_{ch}) \exp\left(-\frac{x - x_{Sj}}{\lambda_{ch}}\right) & x_{Sj} < x \end{cases} \quad (6)$$

Notice that $U_P(x)$ has been derived directly from Poisson's equation in the source and in the channel. Therefore, the description of the electrostatics from source to channel are expected to capture the impact of doping concentration and dielectric constant in the source (through W_D), and the effect of size/geometry and dielectric constants in the channel and in the oxide (through λ_{ch}).

2.2.2 Continuous Monolithic Ad-hoc Potential

It is also possible to find a simpler description of the potential from source to channel that captures accurately the impact of λ_{ch} and W_D on the tunneling distance. The ad-hoc analytic potential shown in (7) is proposed as a simple, yet adequate solution without resorting to piecewise functions:

$$U_M(x) = \frac{\phi_s - \phi_{ch}}{1 + \exp\left(\frac{x - x_{Sj}}{\Lambda_S}\right)} + \phi_{ch}, \quad (7)$$

where $U_M(x)$ is the continuous solution of the potential from source to channel, and Λ_S is the *potential decay rate* at the source/channel junction (other parameters has been described above).

According to the requirement that $U_M(x)$ should describe the proper band-bending distance from source to channel (Λ_{S-CH}) the decay rate Λ_S can be shown to be (see details in section A.1 of the appendix):

$$\Lambda_S = \frac{W_{DS} + \lambda_{ch}}{6}. \quad (8)$$

Where $\lambda_{ch} = \sqrt{\frac{\epsilon_{body} t_{body}^2}{\epsilon_{ox} 8} \ln\left(1 + \frac{2t_{ox}}{t_{body}}\right) + \frac{t_{body}^2}{16}}$ (for nanowires), and $W_{DS} \approx \sqrt{\frac{2\epsilon}{qN_s} \alpha(\phi_S - \phi_{ch})}$ (see section A.1 of the appendix for details). Notice that Λ_S is not given by the simple average of W_{DS} and λ_{ch} . The conduction and valence band potential profiles from source to drain for a complete TFET device can be thus obtained based on equation (7) as:

$$\Phi_C(x) = \frac{\phi_S - \phi_{ch}}{1 + \exp\left(\frac{x - x_{Sj}}{\Lambda_S}\right)} + \frac{\phi_{ch} - \phi_D}{1 + \exp\left(\frac{x - (x_{Sj} + L_{eff})}{\Lambda_D}\right)} + \phi_D, \quad (9a)$$

$$\Phi_V(x) = \Phi_C(x) - E_g. \quad (9b)$$

In equation (9) $\Phi_C(x)$ and $\Phi_V(x)$ are the potential profiles of the conduction and valence band respectively along the direction of transport, L_{eff} is the “effective channel length” of the channel ($L_{eff} \approx L_{ch} + \delta x_{Sj} + \delta x_{Dj}$, where L_{ch} is the actual channel length of the device, and δx_{Sj} (δx_{Dj}) is the symmetry shift of the potential at the source/channel (drain/channel) junction, see section A.3 of the Appendix for details), E_g is the bandgap of the semiconductor, the parameters Λ_S and Λ_D are the potential decay rates associated with the source and drain (respectively) as described in equation (8), and ϕ_D is the potential in the drain (the value at the edge of the conduction band). All other parameters have been previously introduced. It is important to point out that the values of ϕ_S and ϕ_D relative to the Fermi Levels in the source/drain (respectively) depend on the doping concentration in those regions and can be found from well-known formulas based on Fermi-Dirac

statistics¹⁸. Moreover, it can be proven that according to (7) the maximum electric field at the source/channel junction ($x = x_{sj}$) is given by (see section A.2 of the appendix for details):

$$E_{\text{Max}} = \frac{\phi_S - \phi_{ch}}{4\Lambda_S} = \frac{\phi_S - \phi_{ch}}{\frac{4}{6}(W_{DS} + \lambda_{ch})}. \quad (10)$$

It is important to note the significant difference between the common assumption of having a maximum electric field $E'_{MAX} = \frac{\phi_S - \phi_{ch}}{\lambda_{ch}}$ and the result shown in (10). In particular, equation (10) supports the argument presented earlier: “When $W_{DS} \geq \lambda_{ch}$ (which is the case for aggressively scaled devices where λ_{ch} is small) the assumption of W_{DS} being negligible is incorrect”. More specifically, assuming $W_{DS} \approx 0$ leads to an overestimation of the electric field ($E'_{MAX} \geq \frac{4}{3} E_{\text{Max}}$), which ultimately translates into a significant error in the calculation of the BTBT current due to its exponential dependence on the strength of the electric field. Although the effect of doping on TFET performance has been pointed out in previous work¹⁹, to the best of our knowledge this is the first time that the impact of source/drain doping concentrations are properly integrated into a novel analytical approach considering the ellipticity of evanescent states (discussed later) and validated with state-of-the-art quantum transport simulations. In previous reports dealing with analytic modeling of homojunction TFETs the impact of doping has not been treated properly since it has been either neglected^{13,20,21}, or avoided by introducing directly a numeric value of the electric field without relating it to a realistic doping concentration^{9,12,22–24}. On the other hand, the average electric field given by $E_{\text{avg}} = \frac{\phi_S - \phi_{ch}}{6\Lambda_S}$ (section A.1 of the appendix) allows to relate the potential decay rate (Λ_S) to the total band bending distance (Λ_{S-CH}) through the observation that $6\Lambda_S = \Lambda_{S-CH}$ and consequently $\Lambda_{S-CH} = W_{DS} + \lambda_{ch}$ which implies that $d_{ch} = \lambda_{ch}$ (see Fig. 1b).

3- Numerical Methods

To test the quality of the above analytical potential by comparison with a well-established modeling approach, the self-consistent Poisson-NEGF (Non-Equilibrium Green's Function^{25,26}) methodology has been used within the tight binding (TB) description to simulate various TFETs. Simulations have been performed by our nanodevice simulation tool NEMO^{27,28}. The TB model uses an $sp^3d^5s^*$ basis with nearest-neighbor interaction to describe InAs and Si Hamiltonians²⁹. This TB model captures the band structure of InAs and Si and the effect of confinement accurately⁸.

The choice of InAs as a channel material in this work has been made purely on the basis of its convenience in terms of: 1) availability, 2) exhibiting a direct band gap with a single dominant tunneling path, which allows the use of the Wentzel–Kramer–Brillouin (WKB) approximation⁸, and 3) relatively low bandgap/effective mass, which leads to high BTBT currents. However, the applicability of the proposed model is not restricted to this material system – in fact a comparison with silicon devices is provided as an example of another material system where it is found that the potential profile calculated through the proposed analytical approach is actually in good agreement with the self-consistent simulations. This is shown in section A.5 of the appendix where the results from self-consistent simulations are compared with those obtained from equation (9) in the case of a Si nanowire TFET. This provides support to the claim that equation (9) is applicable to different semiconductors in a general manner.

It is important to point out that because of the choice of low density-of-states (DOS) InAs channel material the relation between channel-potential and gate-voltage is almost one-to-one. If a different semiconductor with high DOS is chosen the model still allows calculating current vs. channel-

potential if a capacitor network (series of oxide, quantum³⁰⁻³², and electrostatic/offset³³ capacitances) is employed to translate the channel-potential into a gate-voltage.

4.- Modeling TFETs

In its most accurate form, the tunneling transmission based on the WKB approximation is expressed as follows:

$$T_{WKB}(E) = \exp\left(-2 \int_{x_{ini}}^{x_{fin}} k_{IM}(x, E) dx\right), \quad (11)$$

Where $k_{IM}(x, E)$ is the imaginary part of the complex crystal momentum wavevector ($k = k_{RE} + ik_{IM}$) as a function of energy and position, and “ x_{ini} ” and “ x_{fin} ” are the initial and final position of carriers in real space, respectively, when they tunnel elastically through the bandgap.

To obtain an accurate analytic expression for $k_{IM}(x, E)$, it is necessary to find an analytical equation for: 1) $k_{IM}(E)$ - which has been shown to be an elliptic curve that can be described using an analytic expression that agrees with rigorous tight-binding simulations within 1.4% error³⁴ (see section A.4 of the appendix) and 2) the potential profile of the conduction/valence bands from source to drain which is described by equations (6) or (9).

Figures 3 shows the comparison between the potential profiles obtained using (6), (9) and self-consistent quantum transport simulations corresponding to a gate-all-around (GAA) InAs nanowire (NW) TFET with aggressively scaled-down dimensions: $t_{ox}=1\text{nm}$ (oxide thickness), $d=3.4\text{nm}$ (diameter of the nanowire), $L_{ch} = 15\text{nm}$ and corresponding geometric scaling length in the channel $\lambda_{ch} \approx 1.36\text{nm}$ calculated as shown in¹⁵ (see device structure in Fig. 3a).

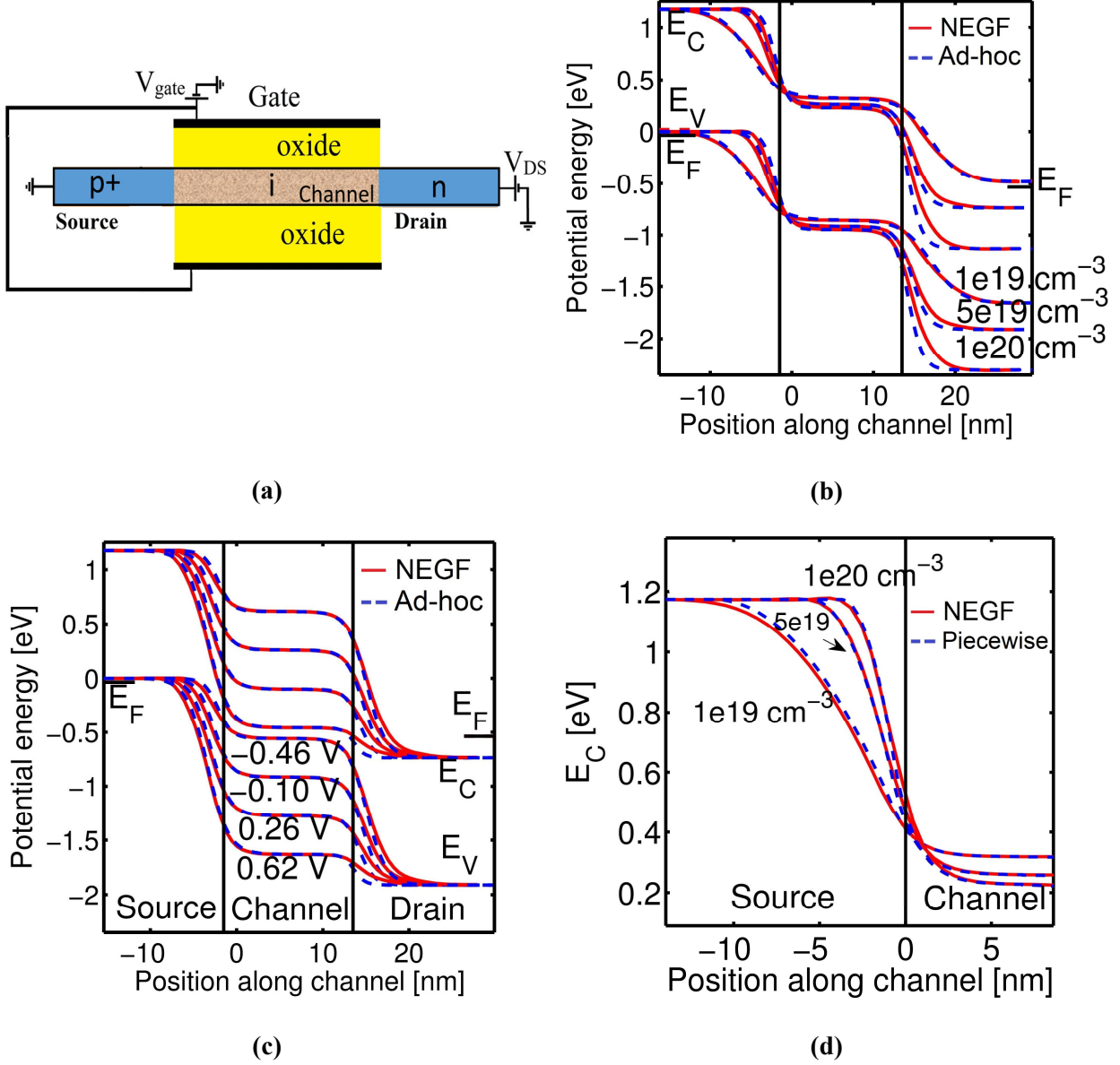


Figure 3. a) Cross section of the simulated device: GAA InAs NW TFET. The ad-hoc potential obtained using equation (9) is compared with state-of-the-art NEGF simulations (red) for: **b)** different doping concentrations (source and drain doping levels are set equal) at a constant gate-voltage ($V_G = -0.1\text{V}$), and **c)** different channel potentials at a constant doping ($N_S = 5 \times 10^{19} \text{cm}^{-3}$). The vertical black lines show the interfaces among the source/channel/drain regions. **d)** Comparison between the analytic piecewise potential

profile described by equation (6) and the results from NEGF simulations for different doping concentrations. The applied drain-voltage is $V_D=0.5V$ in all cases.

In Fig. 3b and 3c the ad-hoc potential approach using equation (9) is compared with NEGF simulations. In Fig. 3b the comparison is made assuming three different doping concentrations in the source/drain regions (source and drain are equally doped) for the same gate-voltage (V_G). In Fig. 3c the comparison is made assuming four different values of V_G while keeping the doping concentration constant. In Fig. 3d the piecewise potential approach using equation (6) is compared with NEGF simulations for three different doping concentrations in the source/drain regions. It is clear from Figs. 3b and 3d that both analytic approaches (ad-hoc and piecewise) are in good agreement with NEGF simulations. Also notice in Figs. 3b and 3d that for all (high) doping concentrations the distance associated with the band-bending inside the source (W_D) is greater than the distance associated with the band-bending inside the channel (d_{ch}). Based on these observations it is clear that accurate calculation of tunneling transmission probabilities in aggressively scaled-down TFETs (where the band-bending inside the gated channel is very small) requires taking into account the band-bending (depletion width) inside the highly doped source/drain as well.

Section A.5 of the appendix shows the comparison between the potential profiles obtained through NEGF simulations and those obtained from equation (9) for a GAA Si NW TFET. Figures 3 and A1 suggest that equation (9) has general applicability and it reproduces with good accuracy the potential landscape of different semiconductors for varying V_G and doping concentrations when compared with the results from NEGF simulations. It is important to point out that appropriate comparison of BTBT currents between the proposed analytic approach and NEGF simulations is not possible in Si nanowires since equation (11) (WKB approximation) provides accurate results

only when is applied to semiconductors with a single dominant tunneling path through the band gap. However, according to previous work this condition is not satisfied in the case of Si nanowires⁸.

The BTBT currents in TFETs can be described using the following analytic model. Using equation (6) or (9) one can write:

$$k_{IM}(x, E_\alpha) = k_{IM}(E = E_\alpha - |q\Phi_V(x)|) , \quad (12)$$

Where $k_{IM}(E)$ is an analytical expression according to Ref. 34 ($k_{IM}(E)$ is shown in appendix A.4 for the sake of clarity and practicality) and E_α is the value of energy at which carriers tunnel elastically between the conduction and valence bands. Then the BTBT “spectral current” (current per unit energy) is essentially given by combining (11) and (12):

$$I_{spect}(E_\alpha) = \frac{2q}{\hbar} \exp\left(-2 \int_{x_{ini}}^{x_{fin}} k_{IM}(x, E_\alpha) dx\right) , \quad (13)$$

where x_{ini} and x_{fin} can be found self-consistently from equation (5) by satisfying the condition $|q\Phi_V(x_{ini})| = |q\Phi_C(x_{fin})| = E_\alpha$. Finally, the total BTBT current is obtained by integrating the spectral current and taking into account the thermal distributions of the Fermi functions:

$$I_{BTBT} = S \cdot \int_{-\infty}^{\infty} I_{spect}(E_\alpha) \left[f_{E,S}(E_\alpha) - f_{E,D}(E_\alpha) \right] dE_\alpha . \quad (14)$$

Where S is the spin degeneracy, and $f_{E,S}$ and $f_{E,D}$ are the Fermi functions at the source and drain respectively.

The model described by equations (13) and (14) enables to calculate the spectral and total tunneling currents respectively both in the on- and off-state of the device for all bias conditions set by ϕ_{ch} and ϕ_D . The parameters required for the calculation are $m_h, m_e, E_g, L_{ch}, \Lambda_S$ and Λ_D . The three first

parameters are material dependent quantities, which are the *confined* hole and electron effective masses, and the *confined* bandgap of the semiconductor, respectively. The three latter are determined by the scaling approach used in the design (dimensions and geometry of both the channel and oxide, and the doping concentrations in the source and drain). Therefore, this analytic model allows to quantitatively explore how a vast variety of parameters (either material-dependent, size and/or geometric) can impact the TFET performance under any bias conditions. Notice that this model describes many relevant tunneling phenomena in TFETs without having to resort to arbitrary fitting parameters or complex numerical methods such as NEGF with high computational burden.

It is important to notice that equation (12) is obtained by combining equations (6) or (9) with equation (A.16) (see section A.5 of the appendix). Since (6), (9) and (A.16) have been shown to be good analytic models for different direct bandgap semiconductors it follows that (13) and (14) should also be applicable and accurate for any direct bandgap semiconductors (with a single dominant tunneling path which allows proper use of the WKB approximation).

5.- Results And Comparisons

Figure 4 shows the validation of the analytic model by comparing the transfer characteristics ($I-V_G$) calculated through NEGF (solid lines), those obtained through the piecewise potential approach by combining (6) and (14) (cross symbols), and those from the ad-hoc potential approach by combining (9) and (14) (circle symbols). The investigated device is the GAA InAs NW TFET described earlier which was simulated to obtain the results presented in Fig. 3. Figure 4a shows the $I-V_G$ for three different doping concentrations (i.e. different W_D) while keeping λ_{ch} constant ($\lambda_{ch} \approx 1.36nm$). Figure 4b is a zoom-in of Fig. 4a revealing more clearly the details of the curves

in the on-state of the device. Figure 4c shows the comparison between I - V_G curves as the relative oxide dielectric permittivity (ϵ) is changed from 2.25 ($\lambda_{ch} \approx 2.3\text{nm}$) to 36 ($\lambda_{ch} \approx 1\text{nm}$) while the source/drain doping concentrations are kept constant (W_D constant). It is clear that the analytic approaches proposed in this work to describe the potential profile (piecewise and ad-hoc) are both found to reproduce with good accuracy the results obtained through NEGF for different values of W_D and λ_{ch} . In addition, notice that the proposed analytic approaches are in good agreement with the NEGF simulations both in the on- and off-state of the device and for both the p- as well as the n-branch of conduction. This shows that an appropriate representation of 1) the variation of the potential profile along the channel including the impact of doping in the source/drain regions, and 2) the elliptic curvature of the evanescent states including the elliptic nature of imaginary branches, provides the means to describe the main physical phenomena related to BTBT in TFETs.

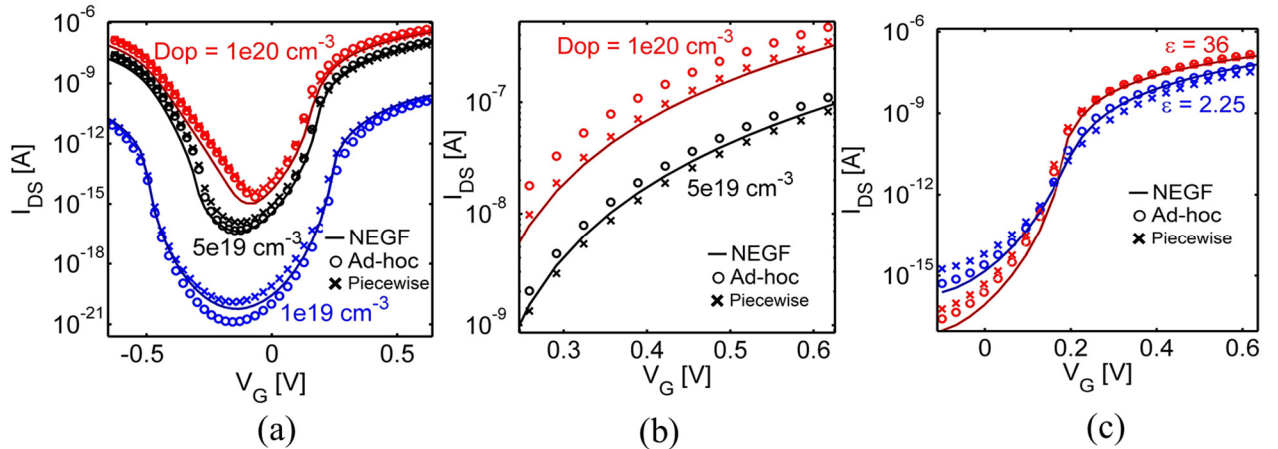


Figure 4. Comparison of transfer characteristics for **a)** three different doping concentrations while keeping λ_{ch} constant ($\lambda_{ch} \approx 1.36\text{nm}$), **b)** zoomed in plot of **a**, and **c)** two different oxide dielectric permittivities (i.e., two different values of λ_{ch}) while the source/drain doping concentrations are kept constant ($N_S=5 \times 10^{19}\text{cm}^{-3}$). The applied drain voltage is $V_D=1\text{V}$. The figure shows the results obtained through NEGF (solid lines), those obtained through the piecewise potential approach by combining (6) and (14)

(cross symbols), and those from the ad-hoc potential approach by combining (9) and (14) (circle symbols). The simulated device is a GAA InAs NW TFET (same structure as shown in Fig. 2a).

In previous publications an expression based on the Fowler-Nordheim (FN) approach given by

$$T_{WKB}^{FN} \approx \exp\left(-\frac{4\lambda_{ch}\sqrt{2m_{red}^*E_g^{3/2}}}{3\hbar(E_g+\Delta E_{ch})}\right)$$

has been frequently used as a means to estimate the BTBT current in TFETs^{1,2,13,20,30}. This implies that equation (11) has been simplified by assuming that: 1) there is a constant electric field in the entire tunneling region (E_0), which can be approximated by $E_0 \approx (E_g + \Delta E_{ch})/q\lambda_{ch}$ (i.e., $\Lambda_{S-CH} \approx \lambda_{ch}$), and 2) carriers tunnel between valence and conduction band with a reduced effective mass given by $m_{red}^* = \frac{m_e m_h}{m_h + m_e}$. Although these assumptions may be fair in the case of Schottky-Barrier (SB) FETs (metal-semiconductor tunneling junctions)^{2,30}, in the case of tunneling homojunctions^{1,13,20} such assumptions may lead to a significant overestimation of the electric field at the junction, which consequently produces vast errors in the calculation of the BTBT currents. Table 1 shows the comparison of the BTBT on-currents (for the same overdrive voltage) estimated using: 1) the FN approach, 2) equation (14) combined with (6) and (9), i.e., using the piecewise and ad-hoc potential approaches (respectively), and 3) NEGF simulations for the same doping concentrations in the source as shown in Figure 3. Notice that the FN approach severely overestimates the on-current by as much as 4 orders of magnitude for a high doping of $N_S=1 \times 10^{19} \text{cm}^{-3}$. As the doping is further increased up to the level of $N_S=1 \times 10^{20} \text{cm}^{-3}$ the error from using the FN approach becomes less dramatic as expected. It is noteworthy that the results of the analytic model follow the same trends as those from NEGF (e.g. several orders of magnitude change in ON-current due to change in the source/drain doping).

Table 1. Comparison of on-currents calculated through different methods for the same device simulated in Figs. 3 and 4. The gate overdrive voltage and doping concentrations are specified in each case.

	ON-CURRENT (A) ($N_S=1 \times 10^{19} \text{cm}^{-3}$) ($V_G - V_{Th} = 0.4 \text{V}$)	ON-CURRENT (A) ($N_S=1 \times 10^{20} \text{cm}^{-3}$) ($V_G - V_{Th} = 0.4 \text{V}$)
Fowler-Nordheim	6.4×10^{-6}	6.4×10^{-6}
Ad-hoc potential	1.3×10^{-10}	4.6×10^{-7}
Analytic potential	1.75×10^{-10}	3.5×10^{-7}
NEGF	2.2×10^{-10}	3.1×10^{-7}

Finally, it is instructive to realize that equation (13) provide the means to perform an energy-dependent analysis of BTBT currents in TFETs. Therefore, the proposed model can be used as a powerful resource to gain both qualitative and quantitative insight into the details of how carriers tunnel as a function of energy, depending on the specific bias conditions. In section A.6 of the appendix it is shown how equation (13) allows to inspect in great detail the dynamics of tunneling carriers. This enables e.g. to understand that at low drain bias the off-current of the device: 1) is given by direct tunneling from source to drain through the gated region, and 2) it mimics the function $k_{IM}(E)$ within the bandgap of the semiconductor. These two conditions may lead to a vast deterioration of the inverse subthreshold slope (S), which is one of the most relevant aspects of design in TFETs.

7.- Conclusions

A new compact model has been developed for the calculation of BTBT currents in high-performance (aggressively scaled-down) ballistic TFETs which use direct bandgap semiconductors with a single dominant tunneling path as channel material. The analytic data was calculated through the use of two different approaches which describe the potential profile from

source to channel including the impact of doping concentration in the source: a piecewise approach based on the solution to the Poisson's equation, and an ad-hoc potential which describes accurately the tunneling distance. Both approaches were found to be in good agreement with the results obtained from state-of-the-art NEGF simulations in all regions of operation of the device, i.e., the on- and off-state, and the p- as well as the n-branch of conduction. The results reveal that the representation of: 1) the potential profile along the channel (including the impact of doping), and 2) the evanescent states through the bandgap (including the ellipticity of the imaginary branch), describe the main physical phenomena related to BTBT in TFETs. It has been shown that as TFETs are aggressively scaled down to improve their performance the depletion width in the source/drain regions has a stronger impact on the TFET performance compared with the effect of the geometric screening length, which is an aspect that has not been taken into account before in TFET modeling. The simplicity and accuracy of the model makes it attractive to explore how a wide variety of parameters (material-dependent, size and/or geometric) can impact the TFET performance under any bias conditions without having to resort sophisticated numerical methods such as NEGF, which have high computational complexity. Moreover, the developed compact model allows to perform an energy-dependent analysis of BTBT currents in TFETs, a powerful resource to study the underlying device physics in various TFETs.

Acknowledgements

This work was supported in part by the Center for Low Energy Systems Technology (LEAST), one of six centers of STARnet, a Semiconductor Research Corporation program sponsored by MARCO and DARPA. The use of nanoHUB.org computational resources operated by the Network for Computational Nanotechnology funded by the US National Science Foundation under

grant EEC-1227110, EEC-0228390, EEC-0634750, OCI-0438246, and OCI-0721680 is gratefully acknowledged.

APPENDIX A

A.1: Decay Rate Of The Analytic Potential Profile

Consider the proposed solution for the potential profile along the channel:

$$U(x) = \frac{\phi_S - \phi_{ch}}{1 + \exp\left(\frac{x - x_{sj}}{\Lambda_S}\right)} + \phi_{ch} . \quad (\text{A.1})$$

where x_{sj} is the position of the source/channel interface, ϕ_S and ϕ_{ch} are the source and channel potentials far from x_{sj} , and Λ_S is the *potential decay rate* at the source/channel junction. Notice that $U(x)$ as shown in (A.1) has first and second derivatives which are continuous at the junction ($x = x_{sj}$). The parameter Λ_S has to be chosen such that it keeps consistency with the underlying physics of the structure. Next, it is discussed how to choose the appropriate value for Λ_S :

It has already been established in previous work¹⁷ that the solution to Poisson's equation inside the gated region can be written as:

$$U_{ch}(x) = (\phi_j - \phi_{ch}) \exp\left(-\frac{x - x_{sj}}{\lambda_{ch}}\right) + \phi_{ch} , \quad (\text{A.2})$$

where ϕ_j is the potential at the source/channel junction. Consider the change in potential " U'_{ch} " defined as $U'_{ch} = U_{ch} - \phi_{ch} = (\phi_j - \phi_{ch}) \exp\left(-\frac{x - x_{sj}}{\lambda_{ch}}\right)$. Then the average change in channel potential " $\langle U'_{ch} \rangle$ " is given by:

$$\langle U'_{ch} \rangle = \frac{1}{(\phi_j - \phi_{ch})} \int_{\phi_{ch}}^{\phi_j} U'_{ch} dU'_{ch} = \frac{1}{(\phi_j - \phi_{ch})} \int_{-\infty}^{x_{sj}} U'_{ch} \frac{\partial U'_{ch}}{\partial x} dx = \frac{(\phi_j - \phi_{ch})}{2} , \quad (\text{A.3})$$

On the other hand, according to (A.2) the electric field is given by:

$$\frac{\partial U_{ch}}{\partial x} = -\frac{(\phi_j - \phi_{ch})}{\lambda_{ch}} \exp\left(-\frac{x - x_{sj}}{\lambda_{ch}}\right), \quad (\text{A.4})$$

The average electric field “ $\langle E_{ch} \rangle$ ” inside the gated channel can then be calculated as follows:

$$\langle E_{ch} \rangle = \frac{1}{(\phi_j - \phi_{ch})} \int_{\phi_{ch}}^{\phi_j} \frac{\partial U_{ch}}{\partial x} dU_{ch} = \frac{1}{(\phi_j - \phi_{ch})} \int_{-\infty}^{x_{sj}} \frac{\partial U_{ch}}{\partial x} \frac{\partial U_{ch}}{\partial x} dx = -\frac{(\phi_j - \phi_{ch})}{2\lambda_{ch}}, \quad (\text{A.5})$$

The distance associated with the band-bending inside the gated channel (see “ d_{ch} ” in Fig. 1b) is assumed to be an average quantity defined by the ratio between $\langle U'_{ch} \rangle$ and $\langle E_{ch} \rangle$ (in magnitude). Therefore, according to (A.3) and (A.5):

$$d_{ch} = \left| \frac{\langle U'_{ch} \rangle}{\langle E_{ch} \rangle} \right| = \lambda_{ch}. \quad (\text{A.6})$$

Thus, the total band bending distance (see “ Λ_{S-CH} ” in Fig. 1) is given by:

$$\Lambda_{S-CH} = W_D + d_{ch} = W_D + \lambda_{ch}. \quad (\text{A.7})$$

Where W_D is the depletion width inside the source region. On the other hand, the average electric field given by (A.1) can be calculated following a procedure analogous to that shown in (A.5):

$$\langle E \rangle = \frac{1}{\phi_s - \phi_{ch}} \int_{\phi_{ch}}^{\phi_s} \frac{\partial U}{\partial x} dU = \frac{1}{\phi_s - \phi_{ch}} \int_{-\infty}^{+\infty} \frac{\partial U}{\partial x} \frac{\partial U}{\partial x} dx = -\frac{\phi_s - \phi_{ch}}{6\Lambda_S}, \quad (\text{A.8})$$

The denominator in the right hand side of (A.8) represents the average distance over which the total potential (i.e. $\phi_s - \phi_{ch}$) drops from source to channel when (A.1) is used to describe the potential profile. Hence, by combining (A.7) and (A.8) it is concluded that $6\Lambda_S = W_D + \lambda_{ch}$ and therefore the potential decay rate is given by:

$$\Lambda_S = \frac{W_D + \lambda_{ch}}{6}. \quad (\text{A.9})$$

The value of W_D is given by the classical expression:

$$W_D = \sqrt{\frac{2\epsilon}{qN_s} \alpha (\phi_s - \phi_{ch})}. \quad (\text{A.10})$$

Where ϵ is the permittivity of the semiconductor, N_s is the doping in the source and α is a number used to satisfy the condition $\alpha(\phi_s - \phi_{ch}) \approx (\phi_s - \phi_j)$ and thus $\alpha \approx (\phi_s - \phi_j)/(\phi_s - \phi_{ch})$. Although strictly speaking α depends on the conditions of the problem it is found to be close to a constant value which is $\alpha \approx 0.6$ and small deviations from this number do not change significantly the results since it has a squared root dependence. The expression shown in (A.10) is valid in the on-state of the device and is ultimately justified by the fact that it matches very well the results obtained from NGEF (as shown in the discussion). In the off-state where BTBT takes place directly between source and drain, the values of Λ_s and W_D are no longer relevant. Therefore, (A.10) is adequate both in the on- and off-state of the TFET.

A.2 : Calculation of Maximum Electric Field

To find maximum magnitude of electric field ($\frac{\partial U}{\partial x}$), the second derivative of (A.1) is evaluated:

$$\frac{\partial^2 U(x)}{\partial x^2} = (\phi_s - \phi_{ch}) \frac{\exp\left(\frac{x+x_{sj}}{\Lambda_s}\right) \left(\exp\left(\frac{x}{\Lambda_s}\right) - \exp\left(\frac{x_{sj}}{\Lambda_s}\right) \right)}{\Lambda_s^2 \left(\exp\left(\frac{x_{sj}}{\Lambda_s}\right) + \exp\left(\frac{x}{\Lambda_s}\right) \right)^3}, \quad (\text{A.11})$$

At $x = x_{sj}$ (A.11) is zero and thus:

$$|E_{Max}| = \left| \frac{\partial U}{\partial x} \right|_{x_{sj}} = \frac{(\phi_s - \phi_{ch})}{4\Lambda_s}. \quad (\text{A.12})$$

A.3: Calculation Of The “Effective Channel Length” (L_{eff})

Equation (A.1) implies that the analytic potential profile is symmetrical with respect to the junction ($x = x_{sj}$). However, the actual potential profile is not symmetric when $W_D \neq \lambda_{ch}$. In this case (where $W_D \neq \lambda_{ch}$), the symmetry point of potential shifts toward the source whenever W_D is larger than λ_{ch} and toward the gate otherwise. Notice that the effective channel length (L_{eff}) does not affect the on-state performance because most of the tunneling takes place around the junction ($x = x_{sj}$) from source to channel (or channel to drain). However, in the off-state of the device most of the tunneling takes place directly from source to drain. Therefore, in the off-state the value of L_{eff} is important and thus the actual position of the junctions (which ultimately determine the

value of L_{eff}) must be properly defined. To account for this effect in equation (A.1), the symmetry point of the junction is shifted according to the difference of W_{DS} and λ_{ch} :

$$\delta x_{Sj} \approx \frac{W_{DS} - \lambda_{ch}}{2}, \quad (\text{A.13})$$

$$\delta x_{Dj} \approx \frac{W_{DD} - \lambda_{ch}}{2}, \quad (\text{A.14})$$

Where δx_{Sj} and δx_{Dj} are the symmetry corrections at the source and drain junctions respectively, and W_{DS} and W_{DD} are the depletion widths corresponding to source and drain respectively. Notice that the shift is zero when the W_{DS} and λ_{ch} are equal. Thus the value of L_{eff} can be taken as:

$$L_{eff} \approx L_{ch} + \delta x_{Sj} + \delta x_{Dj}. \quad (\text{A.15})$$

A.4: Analytic Description of Elliptic Evanescent (Complex) States

In previous research work it has been demonstrated that the evanescent states denoted as “ $k_{IM}(E)$ ” are described by an elliptic curve which can be approximated using a highly accurate analytic formula (within 1.4% error compared to rigorous tight-binding simulations)³⁴. Such formula requires as input the values of the bandgap of the semiconductor E_g , and the corresponding hole and electron effective masses (m_h and m_e respectively). The analytic expression for $k_{IM}(E)$ is repeated here for the sake of clarity:

$$k_{IM}(E) = \frac{1}{\hbar} \sqrt{2m_h E \left(1 - \frac{E}{2E_q}\right)}, \quad \text{for } 0 < E < E_q \quad (\text{A.16a})$$

$$k_{IM}(E) = \frac{1}{\hbar} \sqrt{2m_e (E_g - E) \left(1 - \frac{E_g - E}{2(E_g - E_q)}\right)}. \quad \text{for } E_q < E < E_g \quad (\text{A.16b})$$

Where

$$E_q = E_g \frac{m_e}{m_h + m_e}. \quad (\text{A.16c})$$

In equation (A.16c) the value of E_q is known as the “branching point” and it represents the point in energy inside the bandgap where the carrier changes from hole to electron behavior (or vice versa).

A.5: General Applicability Of The Analytic Model For The Potential Profile

In order to show the general applicability of equation (5), Fig. A1 shows the comparison between the potential profiles obtained through self-consistent simulations and that obtained through (5) for a different channel material. The simulated device is a gate-all-around silicon nanowire TFET with aggressively scaled-down dimensions: (SiO₂ thickness) $t_{ox}=1\text{nm}$, $d=4\text{nm}$ (diameter of the nanowire), $L_{ch} = 20\text{nm}$. According to the results shown in Figs. 2 and A1 equation (5) seems to describe accurately the change in the potential along the channel for different ϕ_{ch} , different doping concentrations, and for different materials when compared with the results obtained from rigorous NEGF simulations.

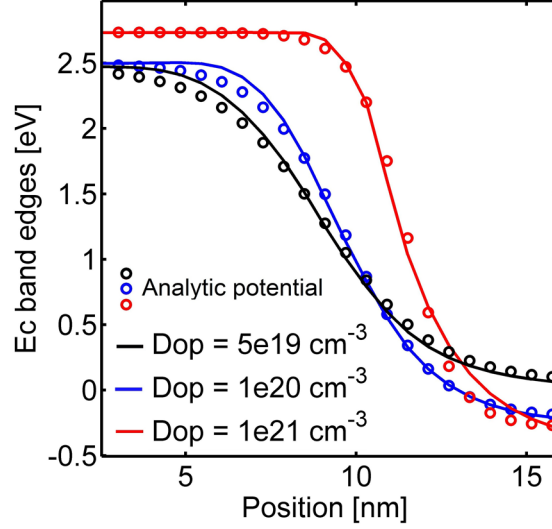


Figure A1. Conduction band potential profiles as a function of position along the channel. The simulated device is a Si nanowire gate-all around TFET. The source/channel interface is located at $x_{sj}=10\text{nm}$. Solid lines are results obtained from NEGF and symbols are values calculated through equation (5).

A.6: Spectral Current Obtained From The Compact Model

Figure A2a shows the transfer characteristic obtained through equation (10) of a hypothetical ballistic device (see parameters in Fig. A2). Figures A2b-A2f show the spectral currents calculated through (9) corresponding band diagrams for some bias points indicated in Fig. A2a. The color bar represents the value of transmission probability for a particular value of energy (i.e., $T_{WKB}(E_\alpha)$).

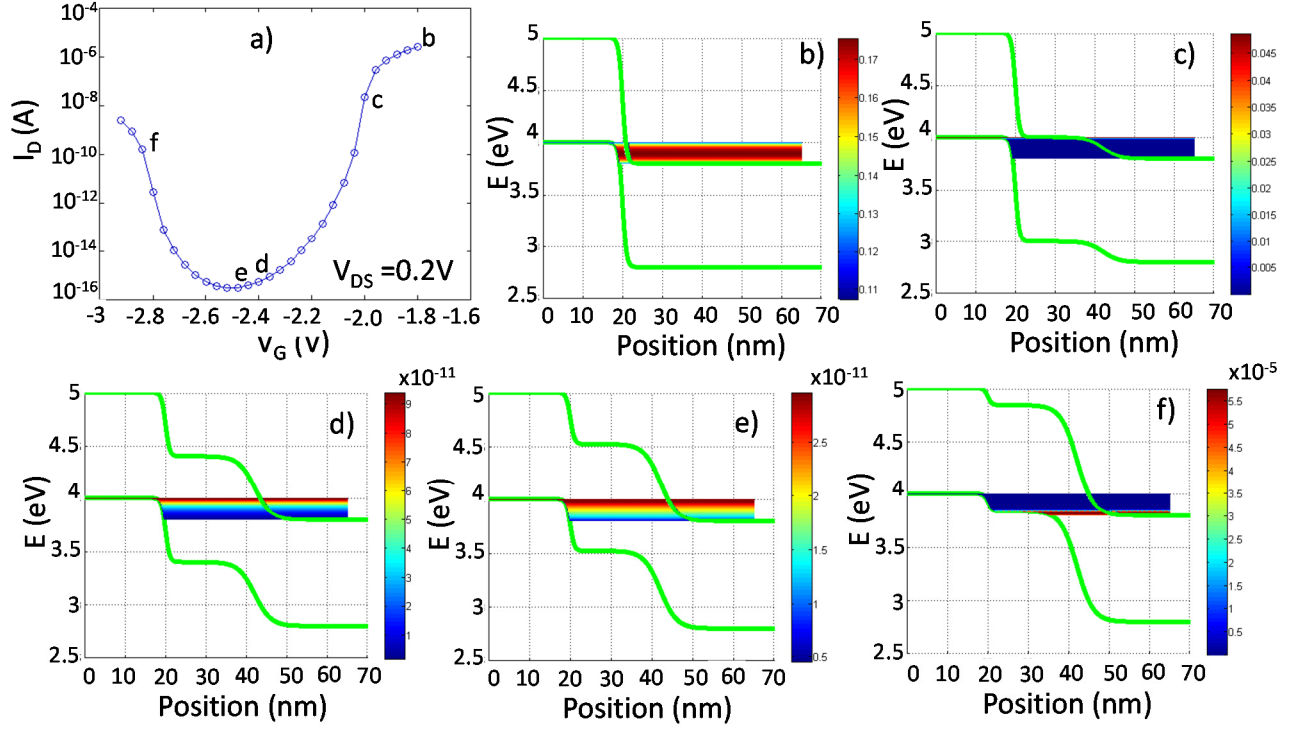


Figure A2. **a)** Transfer characteristic of a hypothetical ballistic TFET obtained through equation (10). The parameters of the device are: $\phi_D = 1V$, $m_h = 0.038m_0$, $m_e = 0.04m_0$, $E_g = 1eV$, $L_{ch} = 30nm$, $\Lambda_S = 2nm$, and $\Lambda_D = 5nm$. **b-f)** Band diagrams for the bias points indicated in A2a calculated with equation (9). The color bar represents the value of $T_{WKB}(E_\alpha)$ for a particular energy in the band diagram. For simplicity it has been assumed that $(f_{E,S} - f_{E,D}) \cdot S = 1$.

Notice that the BTBT current values between points **b** and **c** is due to carriers tunneling from source to channel. But the current between points **c** and **e** is due to carriers tunneling directly from source to drain, which causes a dramatic deterioration of the subthreshold slope (S) deep in the off-state (close to points **d** and **e**). This is highly undesirable because a very steep S (lower than 60mV/dec) is one of the most attractive features of TFETs. Notice that by inspecting only the transfer characteristic it is difficult to understand why S gets deteriorated deep in the off-state, but it becomes clear when looking at the spectral currents at different bias conditions. All BTBT

current values between **e** and **f** also correspond to carriers tunneling directly from source to drain. It is very important to note that the upturn in the transfer characteristics between **e** and **f** is not related to turning on the channel/drain tunneling junction. Instead the upturning is due to the increase of $k_{IM}(E)$ corresponding to carriers tunneling through the bandgap which reflects in the magnitude of the BTBT current. Only in points beyond **f** the BTBT current is dominated by carriers tunneling from channel to drain and this is what gives rise to the actual p-branch of conduction in the transfer characteristic. This is another relevant observation derived from inspecting the spectral current: for aggressively scaled devices at low drain bias the BTBT off-current leakage (from source to drain) mimics the function $k_{IM}(E)$ within the bandgap.

References

- ¹ A.M. Ionescu and H. Riel, *Nature* **479**, 329 (2011).
- ² J. Appenzeller, J. Knoch, M.T. Bjork, H. Riel, H. Schmid, and W. Riess, *IEEE Trans. Electron Devices* **55**, 2827 (2008).
- ³ J. Knoch, S. Mantl, and J. Appenzeller, *Solid. State. Electron.* **51**, 572 (2007).
- ⁴ J. Appenzeller, Y.-M. Lin, J. Knoch, and P. Avouris, *Phys. Rev. Lett.* **93**, 196805 (2004).
- ⁵ J. Knoch and J. Appenzeller, in *63rd Device Res. Conf. Dig. 2005. DRC '05.* (IEEE, 2005), pp. 153–156.
- ⁶ A.Z. Q., Z. W., and Seabaugh, *IEEE Electron Device Lett.* **27**, 297 (2006).
- ⁷ H. Ilatikhameneh, Y. Tan, B. Novakovic, G. Klimeck, R. Rahman, and J. Appenzeller, *Tunnel Field-Effect Transistors in 2D Transition Metal Dichalcogenide Materials*, DOI: [10.1109/JXCDC.2015.2423096](https://doi.org/10.1109/JXCDC.2015.2423096), *arXiv:1502.01760*. (2015).
- ⁸ M. Luisier and G. Klimeck, *J. Appl. Phys.* **107**, (2010).
- ⁹ M.A. Khayer and R.K. Lake, *Appl. Phys. Lett.* **95**, 7 (2009).

- ¹⁰ M. Graef, T. Holtij, F. Hain, A. Kloes, and B. Iñiguez, in *Mix. Des. Integr. Circuits Syst. (MIXDES), Proc. 20th Int. Conf.* (IEEE, 2013), pp. 81–85.
- ¹¹ Q. Zhang, Y. Lu, C.A. Richter, D. Jena, and A. Seabaugh, *IEEE Trans. Electron Devices* **61**, 2719 (2014).
- ¹² A.C. Seabaugh and Q. Zhang, *Proc. IEEE* **98**, 2095 (2010).
- ¹³ R.K. Ghosh and S. Mahapatra, *IEEE J. Electron Devices Soc.* **1**, 175 (2013).
- ¹⁴ R.-H. Yan, A. Ourmazd, and K.F. Lee, *IEEE Trans. Electron Devices* **39**, 1704 (1992).
- ¹⁵ C.P. Auth and J.D. Plummer, *IEEE Electron Device Lett.* **18**, 74 (1997).
- ¹⁶ H. Ilatikhameneh, G. Klimeck, J. Appenzeller, and R. Rahman, *Scaling Theory of Electrically Doped 2D Transistors*, DOI:10.1109/LED.2015.2436356, <http://arxiv.org/abs/1504.03387>. (IEEE, 2015).
- ¹⁷ T. Dutta, Q. Rafhay, G. Pananakakis, and G. Ghibaudo, in *2013 14th Int. Conf. Ultim. Integr. Silicon* (IEEE, 2013), pp. 69–72.
- ¹⁸ R. Kim and M. Lundstrom, *Notes on Fermi-Dirac Integrals*, <http://arxiv.org/abs/0811.0116> (2008).
- ¹⁹ J.T. Smith, C. Sandow, S. Das, R.A. Minamisawa, S. Mantl, and J. Appenzeller, *IEEE Trans. Electron Devices* **58**, 1822 (2011).
- ²⁰ X.-W. Jiang and S.-S. Li, *Appl. Phys. Lett.* **104**, 193510 (2014).
- ²¹ A.S. Verhulst, B. Sorée, D. Leonelli, W.G. Vandenberghe, and G. Groeseneken, *J. Appl. Phys.* **107**, 024518 (2010).
- ²² D. Jena, in *Proc. IEEE* (IEEE, 2013), pp. 1585–1602.
- ²³ N. Ma and D. Jena, *Appl. Phys. Lett.* **102**, 132102 (2013).
- ²⁴ D. Sarkar, M. Krall, and K. Banerjee, *Appl. Phys. Lett.* **97**, 2 (2010).
- ²⁵ S. Datta, *Electronic Transport in Mesoscopic Systems* (Cambridge University Press, 1995).
- ²⁶ R. Lake and S. Datta, *Phys. Rev. B* **45**, 6670 (1992).
- ²⁷ S. Steiger, M. Povolotskyi, H.-H. Park, T. Kubis, and G. Klimeck, *IEEE Trans. Nanotechnol.* **10**, 1464 (2011).

- ²⁸ J.E. Fonseca, T. Kubis, M. Povolotskyi, B. Novakovic, A. Ajoy, G. Hegde, H. Ilatikhameneh, Z. Jiang, P. Sengupta, Y. Tan, and G. Klimeck, *J. Comput. Electron.* **12**, 592 (2013).
- ²⁹ T.B. Boykin, G. Klimeck, R.C. Bowen, and F. Oyafuso, *Phys. Rev. B* **66**, 125207 (2002).
- ³⁰ J. Knoch and J. Appenzeller, *Phys. Status Solidi* **205**, 679 (2008).
- ³¹ R.B. Salazar, S.R. Mehrotra, G. Klimeck, N. Singh, and J. Appenzeller, *Nano Lett.* **12**, 5571 (2012).
- ³² S. Ilani, L.A.K. Donev, M. Kindermann, and P.L. McEuen, *Nat. Phys.* **2**, 687 (2006).
- ³³ E.F. Schubert, R.F. Kopf, J.M. Kuo, H.S. Luftman, and P.A. Garbinski, *Appl. Phys. Lett.* **57**, 497 (1990).
- ³⁴ X. Guan, D. Kim, K.C. Saraswat, and H.-S.P. Wong, *IEEE Electron Device Lett.* **32**, 1296 (2011).